

Transmission of plasmons through a nanowire

Peter Geisler,^{1,*} Enno Krauss,^{1,*} Gary Razinskas,^{1,*} and Bert Hecht^{1,2,†}

¹*NanoOptics & Biophotonics Group, Experimentelle Physik 5, Physikalisches Institut, Universität Würzburg, Am Hubland, 97074 Würzburg, Germany*

²*Röntgen Research Center for Complex Material Systems (RCCM), Am Hubland, 97074 Würzburg, Germany*
(Dated: 2022-02-03)

Exact quantitative understanding of plasmon propagation along nanowires is mandatory for designing and creating functional devices. Here we investigate plasmon transmission through top-down fabricated monocrystalline gold nanowires on a glass substrate. We show that the transmission through finite-length nanowires can be described by Fabry-Pérot oscillations that beat with free-space propagating light launched at the incoupling end. Using an extended Fabry-Pérot model, experimental and simulated length dependent transmission signals agree quantitatively with a fully analytical model.

At optical frequencies gold and silver nanowires can be used as subwavelength waveguides due to the considerably shortened effective wavelength of surface plasmon polaritons compared to free-space light [1, 2]. Nanowires therefore represent fundamental building blocks of nano-optical circuitry that may find applications in nano quantum optics, information processing and sensing [3–7]. High-precision experiments of simple physical systems often reveal subtle but important effects or can be used to test theoretical descriptions of experimental results. Validated theoretical descriptions can then be used with confidence to model more complex systems. Yet, systematic high-precision experiments of light transmission through nanowires to date hardly exist. For example, the transmission efficiency of light through such nanowires in many experiments significantly deviates from theoretical expectations based on bulk dielectric constants [8, 9]. To date the origin of such deviations remains unknown since the structural uncertainties of bottom up and top-down fabricated nanowires are not small enough to allow for conclusive analyses.

Here we present a systematic study of the monochromatic light transmission through more than 300 monocrystalline gold nanowires of equal cross section but variable length ranging between 1940 to 8040 nm in length with a 20 nm increment. We demonstrate by experiments and simulations that a quantitatively correct description of the length-dependent nanowire transmission can be obtained by also taking into account free-space propagating modes launched by scattering of the excitation spot at the wire input in addition to Fabry-Pérot-type internal plasmon resonances. These free-space propagating modes interact with the outcoupling end of the wire and beat with the regularly emitted photons originating from the wire plasmon's radiative decay. This leads to significant amplitude modulations of the Fabry-Pérot transmission resonances. The quantitative agreement between our model, numerical simulations, and measurements validates our model and yields values of propagation parameters that are compatible with bulk dielectric constants and for which remaining sources

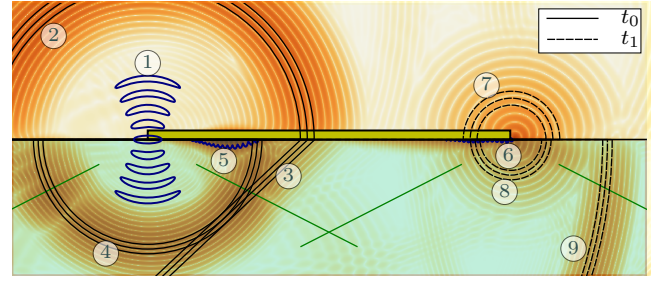


FIG. 1. (color online) Sketch of the free-space and guided fields involved in the experiment in a plane through the nanowire long axis perpendicular to the substrate (wire height stretched for better visibility). The field intensity distributions are represented in a logarithmic scale and were obtained by FDTD simulations. To illustrate progress in time the intensities of two short pulses with a short time delay $t_1 - t_0$ are combined. (1) focused Gaussian source illumination from the glass half space; (2) scattered and transmitted light above the glass surface leading to (3) refracted waves at the air-glass interface; (4) scattered and reflected light below the air-glass interface; (5) launched plasmon pulse at time t_0 ; (6) plasmon pulse at time t_1 ; light emission from the wire end (7) above and (8) below the air-glass interface; (9) scattered and reflected light below the air-glass interface at time t_1 leading to additional scattered fields at the wire end. The (green) lines below the glass surface symbolize the limited accepting angle of the objective with $\text{NA} = 1.3$.

of uncertainties are clearly identified.

To experimentally characterize the transmission properties of nanowires of different lengths we use a home-build inverted microscope setup [10]. Nanofabricated single crystal gold nanowires supported by a cover glass are mounted above an oil immersion microscope objective (Leica, 1.30 NA, ∞ , PL Fluotar 100x) which is used to focus a laser beam ($\lambda = 800$ nm, 12 nm FWHM spectral linewidth, 80 MHz repetition rate, 50 nW average power measured in front of the objective, NKT Photonics, SuperK Power with SpectraK AOTF) via a $\lambda/2$ -plate (Foctec, AWP210H NIR) to a diffraction-limited (390 nm

diameter) spot at the air–glass interface that is linearly polarized along the wire axis. The same objective is used to image the emitted and reflected light onto a CCD camera (Andor, DV887AC-FI EMCCD) via a 50/50 non-polarizing beamsplitter (Thorlabs, CM1-BS013). In order to avoid saturation of the CCD, the strong reflection of the excitation spot is suppressed by a small beam block (OD 2) introduced in an intermediate image plane. The exact position of the excitation spot with respect to the wire end can be adjusted with nm-precision by moving the sample using a piezo translation stage (Physik Instrumente, P-527) and was optimized to obtain maximum signal intensity at the wire end. The principle of the experiment and all light propagation channels are sketched in Fig. 1 showing free-space and guided fields as obtained from numerical simulations. The tightly focused laser at the incoupling end of the wire (Fig. 1(1)) launches a plasmon with about 30% efficiency (Fig. 1(5)) that propagates towards the outcoupling end (Fig. 1(6)) where it is partly radiated into the surrounding media (Fig. 1(7) and (8)) while about 40% of the plasmon field is reflected and propagates back along the wire leading to Fabry-Pérot-type standing waves [11, 12]. Additional propagating fields - in the following referred to as air-wave and glass-wave (Fig. 1(2) and (4)) - are launched by the partial scattering of the excitation source at the incoupling end. While about 30% of the laser energy is coupled into the nanowire, about 50% of the energy is scattered into the glass half space leading to a spherical wave originating from the incoupling end of the wire. The remaining 20% are transmitted into the air half space where they also evolve as spherical waves. Another contribution to propagating waves in the glass half space arises from light refracted at the air–glass interface (Fig. 1(3)) which propagates into the glass as a plane wave under an angle of about 43° (critical angle for total internal reflection) and thus within the acceptance angle of the objective. This wave leads to a distinct pattern in the wire far-field images that vanishes for low-NA imaging. The air-wave and the glass-wave originating from the excitation position are not directly detected by the camera for different reasons. While the air-wave propagates away from the collecting objective lens above the interface the glass-wave is strongly suppressed by the beam block at the intermediate image plane. However, as we detail below, the interaction of these propagating waves of different effective wavelengths with the wire end leads to interference and beating effects in the light intensity emitted by the wire ends which is detected by the camera. A video showing the time evolution of a focused laser pulse coupled to the end of a wire and all resulting free-space and guided fields involved in the experiment can be found in the SI.

Using an eigenmode solver (Lumerical Solutions, MODE Solutions) it can be confirmed that the propagation along the present nanowire is single mode at the cho-

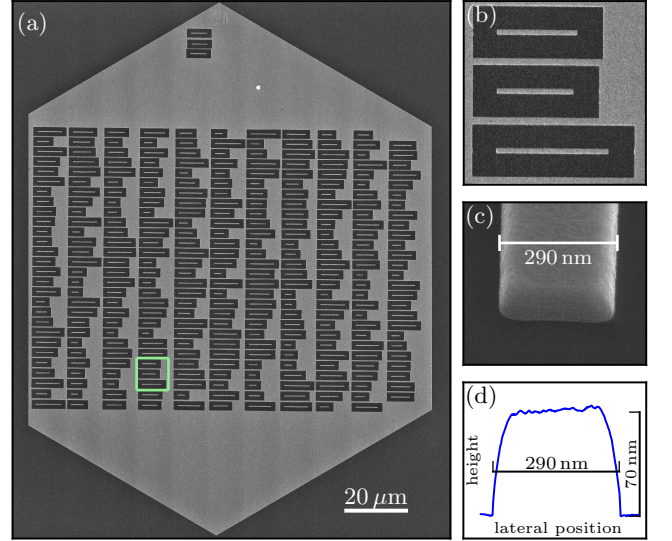


FIG. 2. (color online) (a)-(c) Scanning electron microscopy (SEM) images of the sample showing (a) the full platelet including the focused-ion beam milled area of the platelet with the array of single wires of random wire lengths as well as (b), (c) two closeups at different zoom levels. (d) Atomic force microscopy line profile along one wire's cross section.

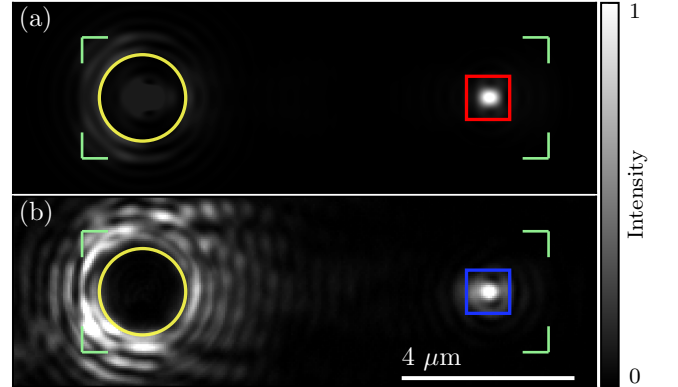


FIG. 3. (color online) (a) Far-field intensity from FDTD simulation of an $8\ \mu\text{m}$ long wire and (b) the corresponding experimental CCD image. The (yellow) circle visualizes the position of the beam block and the (green) corners mark the borders between gold platelet on glass and bare glass (see Fig. 2 and SI). The red (blue) square marks the area that was integrated to obtain the intensity in simulation (experiment). Experimental data was scaled to match simulated peak intensity within the integration area.

sen vacuum wavelength (see SI). Based on Fabry-Pérot theory the field amplitude ψ_T that is transmitted by a waveguide of length L via one single eigenmode and emit-

ted into the detection path can be expressed as [12]

$$\psi_T = \frac{\psi_0 \eta t e^{-(\alpha+i\beta)L}}{1 - (r e^{-(\alpha+i\beta)L})^2}. \quad (1)$$

Here, ψ_0 is the amplitude of the Gaussian excitation beam, η is a (complex valued) efficiency factor comprising the combined effects of incoupling into the waveguide and detecting the emitted signal, and $r = R e^{i\phi}$ and t are the complex plasmon reflection and transmission coefficients, respectively. These coefficients are assumed to be identical for both wire terminations. Furthermore, $\alpha = 1/2l_{\text{decay}}$ and $\beta = 2\pi/\lambda_{\text{eff}}$ denote the propagating wire mode's attenuation and wave number, respectively, with l_{decay} being the mode's intensity decay length and λ_{eff} its effective wavelength. Both air-wave and glass-wave can be approximated by propagating spherical waves. The respective amplitudes scattered from the wire far end at a distance L away from the incoupling end towards the detector can be expressed as

$$\psi_{\text{medium}} = \psi_0 \eta_{\text{medium}} \frac{e^{-i\beta_{\text{medium}}L}}{L}, \quad (2)$$

where $\beta_{\text{medium}} = 2\pi/\lambda_{\text{medium}}$ is the wave vector and λ_{medium} is the wavelength of light in the respective medium, i.e. air and glass. The complex quantity η_{medium} denotes a combined efficiency factor accounting for the efficiency of scattering of the excitation field ψ_0 at the incoupling wire end, thus generating the spherical wave in the respective medium, as well as for the efficiency for scattering of this wave at the wire's far end into the detection path. All fields originating from the waveguide end interfere at the detector according to

$$I_{\text{total}} = |\psi_T + \psi_{\text{air}} + \psi_{\text{glass}}|^2. \quad (3)$$

To perform a high-precision experiment that can reveal the effects of the additional free-space waves on the overall apparent wire transmission we prepared a sample consisting of 306 monocrystalline [13, 14] gold nanowires ranging from 1940 nm to 8040 nm in nominal length with a length increment of 20 nm (Fig. 2). All nanowires were fabricated by focused-ion beam (FIB) milling of a single monocrystalline gold platelet to ensure uniform milling conditions. The wire lengths were distributed randomly over the array to avoid artifacts due to changes of fabrication or measurement conditions. Simulations show that the remaining gold frames (Fig. 2 (b)) around the wires do not affect the in- or outcoupled intensity (see SI). All resulting wires are of uniform quality showing no observable differences in SEM images apart from the wire length. To provide optimal conditions for focused-ion beam milling the sample was fabricated on a conductive substrate (silicon) and then transferred to a clean and flat glass substrate (no adhesion layers). Transfer to the glass substrate avoids the presence of a glass ridge below

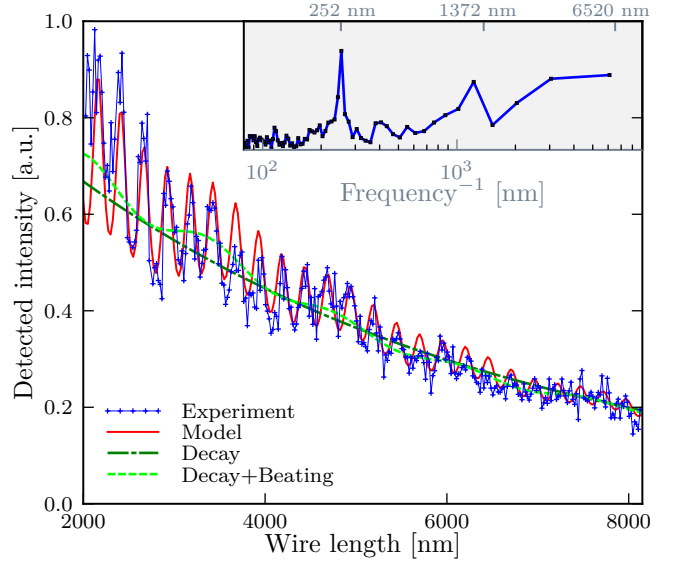


FIG. 4. (color online) Detected signal (blue “x”, thin blue line to guide the eye) within the integration box at the wire end. Superimposed is the fitted model (solid red line) together with the intensity decay curve (interleaved dark green line) and a curve of the model with Fabry-Pérot reflectivity $R = 0$ visualizing the oscillations from the beating between the Fabry-Pérot model and the scattered free-space waves in air and glass at the wire end (dashed light green line); (inlay) Fourier transformed experimental data. The expected peak positions from the Fabry-Pérot oscillation (252 nm), the beating between the transmitted light and the air-wave (1372 nm), and the beating between the transmitted light and the glass-wave (6520 nm) are indicated.

the nanowires and excludes fabrication-induced surface roughness as well as Ga^+ -Ion implantation within the milling area [15]. The simulation results are obtained by modeling the structure using a finite-difference time-domain (FDTD) solver (Lumerical Solutions, FDTD Solutions). The geometry was chosen to match high resolution SEM and AFM images and includes e.g. the soft edges (Fig. 2 (c,d)). Optical properties of the gold are taken from literature [16, 17], while the refractive index of the glass was set to $n = 1.46$. Using the eigenmode solver the fundamental mode properties for the present geometry at vacuum wavelength $\lambda = 800$ nm are calculated to be $\lambda_{\text{eff}} = 505$ nm and $l_{\text{decay}} = 4960$ nm. In order to simulate far-field images of the wire near-field intensities are recorded 10 nm below the structure and projected into the far-field [18, 19]. Simulated and experimentally obtained far-field images for a wire of 8 μm length are displayed in Fig. 3 (a) and (b), respectively. The effect of the beam block used for spatially blocking the high-intensity reflection spot resulting from the focused laser excitation of the nanowire input terminal is visible by the nearly circular areas of reduced intensity around the excitation spot. Apart from a somewhat

increased scattering in the experiment simulated and experimental images agree exceptionally well.

For a detailed analysis of plasmon transmission through the nanowires we extract for each nanowire the simulated far-field intensity as well as experimental CCD image counts by integrating $1\ \mu\text{m} \times 1\ \mu\text{m}$ squares centered at the wire end (red and blue squares in Fig. 3). From all 306 measured nanowires, only about 1% showed unexpected signals that we attribute to structural defects (see SI) and therefore excluded them from the further analysis. The resulting values for the experimentally determined wire transmission are plotted as a function of the wire length (Fig. 4 (blue “x”). A corresponding plot resulting from simulated far-field images can be found in the SI. The data is normalized such that the resulting decay curve (interleaved dark green line) passes an intensity value of $1/e$ at a wire length matching l_{decay} . The detected intensity as a function of the wire length exhibits an exponential decay modulated by an oscillatory behavior. A short-wavelength and a superimposed longer-wavelength oscillation are distinguishable. We compare the experimental data to the proposed model by fitting Eq. 3 to the data. In order to reduce the number of free parameters the mode’s propagation properties ($\lambda_{\text{eff}} = 505\ \text{nm}$, $l_{\text{decay}} = 4960\ \text{nm}$) and its reflection coefficient at the wire termination ($R = 0.42$, $\phi = 1.39$) are obtained from FDFD and FDTD simulation, respectively. The initial phase offsets of both air-wave and glass-wave with respect to the propagating plasmon are set to a fixed value of π . With these constraints the amplitudes of the launched wire plasmon, the air-wave, and the glass-wave at the incoupling position remain the only free parameters of the model. The resulting fit to the simulation data (see SI) shows perfect agreement. The amplitude ratio of the three contributions is adopted from this fit, so that the final fit to the experimental data has only one remaining amplitude parameter. An additional length offset of $85\ \text{nm}$ has to be introduced, which accounts for a systematic difference between the nominal and the actual wire length which is also observed in high-resolution SEM measurements. The model is plotted as a red line in Fig. 4. The Fourier transformation of the length-dependent data (inset of Fig. 4) shows two distinct peaks. The highest frequency component corresponds to a periodicity of $252\ \text{nm}$ and therefore matches $\lambda_{\text{eff}}/2$ as anticipated by the Fabry-Pérot model. The slower oscillation corresponding to a wavelength of about $1300\ \text{nm}$ corresponds to the calculated beating wavelength of the excitation’s vacuum wavelength and the Fabry-Pérot modulated plasmon emission at $\lambda_{\text{beating}}^{\text{air-fpt}} = 1372\ \text{nm}$. We thus attribute it to the interference of the spherical air-wave scattered at the wire end and the emitted plasmons. This origin is further supported by numerical simulations using a mode source to directly excite the plasmons without launching spherical waves and the resulting absence of the beating (see SI). In addition,

the model predicts a beating between the plasmon emission and the glass-wave showing a periodicity of about $\lambda_{\text{beating}}^{\text{glass-fpt}} = 6520\ \text{nm}$. This beating wavelength is about the same as the length-difference between longest and shortest measured wire ($\Delta L_{\text{max}} = 6100\ \text{nm}$) and close to the length scale of the plasmonic intensity decay ($l_{\text{decay}} = 4960\ \text{nm}$). While it is not clearly resolved in the Fourier transformation data it is important to note that - within the observation window - it will appear as an additional slope of the exponential decay curve. Neglecting this additional component would - depending on it’s relative phase - lead to either an under- or overestimation of the decay length. This can best be seen in Fig. 4 by the dashed light green curve which oscillates (visible beating $\lambda_{\text{beating}}^{\text{air-fpt}} = 1372\ \text{nm}$) above the interleaved dark green decay curve because of the additional intensity caused by the beating between the spherical wave in glass and the Fabry-Pérot modulated plasmon emission. To observe and distinguish these different contributions in the experiment the requirements on the sample’s geometrical precision are demanding. By validating our experimental data against a model that includes artificial errors, i.e. by comparing the residuals, we determine the upper limits for the uncertainties (standard deviation) of our structures geometrical parameters and experimental conditions, i.e. wire length, width as well as random intensity fluctuations to be $32\ \text{nm}$, $8\ \text{nm}$ and 7% , respectively (see SI). For the length of the wires this corresponds to a relative error of below 0.4% , which is, taking into account the non-conductive substrate, smaller than the experimentally accessible resolution limit of current state of the art SEM techniques.

We conclude that the high precision and reproducibility of the fabricated nanowires allowed us to reveal the nonnegligible influence of air and substrate waves on their apparent length-dependent transmission. Our experiments also show that by inclusion of these additional waves simulated and experimental data agree quantitatively within the remaining small experimental uncertainties. The effect of the air wave becomes apparent as a beating superimposed to the Fabry-Pérot standing wave pattern. The role of the substrate wave is less obvious. We show that the very long beating wavelength of the substrate wave with the wire plasmon causes unavoidable uncertainty for the fitting of the decay length because the corresponding oscillatory behaviour cannot be captured even for longer wires since the overall damping of the plasmon becomes too strong. The resulting uncertainty regarding the starting phase of the substrate wave is likely responsible for measurements of decay lengths that reported too long or too short decay lengths[8, 9].

* equally contributing

[†] hecht@physik.uni-wuerzburg.de

- [1] L. Novotny and C. Hafner, Phys. Rev. E **50**, 4094 (1994).
- [2] J. Takahara, S. Yamagishi, H. Taki, A. Morimoto, and T. Kobayashi, Optics letters **22**, 475 (1997).
- [3] J. N. Anker, W. P. Hall, O. Lyandres, N. C. Shah, J. Zhao, and R. P. Van Duyne, Nat Mater **7**, 442 (2008).
- [4] D. Martín-Cano, L. Martín-Moreno, F. J. García-Vidal, and E. Moreno, Nano Lett. **10**, 3129 (2010).
- [5] D. E. Chang, A. S. Sørensen, E. A. Demler, and M. D. Lukin, Nat Phys **3**, 807 (2007).
- [6] Y. Fu, X. Hu, C. Lu, S. Yue, H. Yang, and Q. Gong, Nano Lett. **12**, 5784 (2012).
- [7] S. Raza, M. Esfandyarpour, A. L. Koh, N. A. Mortensen, M. L. Brongersma, and S. I. Bozhevolnyi, Nature Communications **7**, 13790 (2016).
- [8] P. Kusar, C. Gruber, A. Hohenau, and J. Krenn, Nano Lett. (2012), 10.1021/nl203452d.
- [9] B. Wild, L. Cao, Y. Sun, B. P. Khanal, E. R. Zubarev, S. K. Gray, N. F. Scherer, and M. Pelton, ACS Nano , 120103091414004 (2012).
- [10] P. Geisler, G. Razinskas, E. Krauss, X.-F. Wu, C. Rewitz, P. Tuchscherer, S. Goetz, C.-B. Huang, T. Brixner, and B. Hecht, Phys. Rev. Lett. **111**, 183901 (2013).
- [11] C. Fabry and A. Pérot, Ann. Chim. Phys. **16**, 115 (1899).
- [12] D. Hofstetter and R. L. Thornton, Opt. Lett. **22**, 1831 (1997).
- [13] J.-S. Huang, V. Callegari, P. Geisler, C. Brünig, J. Kern, J. C. Prangsma, X. Wu, T. Feichtner, J. Ziegler, P. Weinmann, M. Kamp, A. Forchel, P. Biagioni, U. Sennhauser, and B. Hecht, Nat Comms **1**, 150 (2010).
- [14] X. Wu, R. Kullock, E. Krauss, and B. Hecht, Crystal Research and Technology **50**, 595 (2015).
- [15] X. Wu, P. Geisler, E. Krauss, R. Kullock, and B. Hecht, Nanoscale **7**, 16427 (2015).
- [16] P. G. Etchegoin, E. C. Le Ru, and M. Meyer, The Journal of Chemical Physics **125**, 164705 (2006).
- [17] P. G. Etchegoin, E. C. Le Ru, and M. Meyer, The Journal of Chemical Physics **127**, 189901 (2007).
- [18] A. Taflov and S. C. Hagness, *Computational electrodynamics: the finite-difference time-domain method*, 3rd ed., Artech House antennas and propagation library (Artech House, Boston, 2005).
- [19] L. Novotny and B. Hecht, *Principles of nano-optics*, 2nd ed. (Cambridge University Press, Cambridge, 2012).